Magma Storage System and Hidden Hotspot Track of the Emeishan Large Igneous Province and its Impact on the Timing of the Capitanian Mass Extinction

Yiduo Liu[1], Lun Li[2], Jolante Van Wijk[3], Aibing Li[1], and Yuanyuan V Fu[4]

[1]Department of Earth and Atmospheric Sciences, University of Houston
[2]Guangdong Provincial Key Lab of Geodynamics and Geohazards, School of Earth Sciences and Engineering, Sun Yat-sen University
[3]Department of Earth and Environmental Science, New Mexico Institute of Mining and Technology
[4]Key Laboratory of Earthquake Prediction, Institute of Earthquake Forecasting, China Earthquake Administration

November 22, 2022

Abstract

Large igneous provinces (LIPs) are often associated with mass extinctions and are vital for life evolution on Earth. However, the precise relation between LIPs and their impacts on biodiversity is enigmatic as they can be asynchronous. If the environmental impacts are primarily related to sill emplacement, the structure of LIPs' magma storage system becomes critical as it dictates the occurrence and timing of mass extinction. Here we use surface wave tomography to image the lithosphere under the Permian Emeishan Large Igneous Province (ELIP) in SW China. We find a NE-trending zone of high shear-wave velocity (Vs) and negative radial anisotropy (Vsv > Vsh) in the crust and lithosphere and interpret it as a mafic-ultramafic, dike-dominated magma storage system on the hidden hotspot track of the ELIP. An area of less-negative radial anisotropy, on the hotspot track but away from the eruption center, reflects an elevated proportion of sills emplaced at the incipient stage of the ELIP. Liberation of poisonous gases and mercury by the sills explains why the mid-Capitanian global biota crisis preceded the peak ELIP eruption by 2-3 million years.

1 # Magma Storage System and Hidden Hotspot Track of the

2 # Emeishan Large Igneous Province and its Impact on the Timing

3 # of the Capitanian Mass Extinction

4

5 **Yiduo Liu[1, 6], Lun Li[2, 3, 6], Jolante van Wijk[4], Aibing Li[1], Yuanyuan V. Fu[5]**

6

7 [1] *Department of Earth and Atmospheric Sciences, University of Houston, Houston, Texas 77204,*

8 *USA*

9 [2] *Guangdong Provincial Key Lab of Geodynamics and Geohazards, School of Earth Sciences*

10 *and Engineering, Sun Yat-sen University, Guangzhou, Guangdong 510275, China*

11 [3] *Southern Marine Science and Engineering Guangdong Laboratory (Zhuhai), Zhuhai,*

12 *Guangdong 510999, China*

13 [4] *Department of Earth and Environmental Science, New Mexico Institute of Mining and*

14 *Technology, Socorro, New Mexico 87801, USA*

15 [5] *Key Laboratory of Earthquake Prediction, Institute of Earthquake Forecasting, China*

16 *Earthquake Administration, Beijing, 100036, China*

17 [6] *These authors contributed equally. Correspondence to: Lun Li (lilun6@mail.sysu.edu.cn).*

18

19 **ABSTRACT**

20   Large igneous provinces (LIPs) are often associated with mass extinctions and are vital

21 for life evolution on Earth. However, the precise relation between LIPs and their impacts on

22 biodiversity is enigmatic as they can be asynchronous. If the environmental impacts are primarily

23   related to sill emplacement, the structure of LIPs' magma storage system becomes critical as it

24   dictates the occurrence and timing of mass extinction. Here we use surface wave tomography to

25   image the lithosphere under the Permian Emeishan Large Igneous Province (ELIP) in SW China.

26   We find a NE-trending zone of high shear-wave velocity (Vs) and negative radial anisotropy

27   (Vsv > Vsh) in the crust and lithosphere and interpret it as a mafic-ultramafic, dike-dominated

28   magma storage system on the hidden hotspot track of the ELIP. An area of less-negative radial

29   anisotropy, on the hotspot track but away from the eruption center, reflects an elevated

30   proportion of sills emplaced at the incipient stage of the ELIP. Liberation of poisonous gases and

31   mercury by the sills explains why the mid-Capitanian global biota crisis preceded the peak ELIP

32   eruption by 2-3 million years.

33

34   **INTRODUCTION**

35   Large igneous provinces are characterized by rapid emplacement of predominantly mafic

36   magma in the lithosphere and volcanic eruptions forming plateau basalts in an area greater than

37   10^5 km^2 (Bryan and Ernst, 2008). Many LIPs have been associated with abrupt environmental

38   catastrophes and mass extinction events (Sobolev et al., 2011; Ernst, 2014). While several LIP-

39   related extinctions occurred during or shortly after the major volcanic phase of the corresponding

40   LIPs (Bond and Wignall, 2014), some preceded the major phase, leaving an enigma on the exact

41   temporal relationship between LIPs and the associated mass extinctions.

42   The structure of magma storage systems of LIPs, particularly sill emplacement, is a key

43   to understanding this relation (Svensen et al., 2009). Modern hotspots, such as Yellowstone,

44   display the magma storage system of actively forming LIPs (Jiang et al., 2018). However, they

45   do not provide direct constraint on the timing of mass extinction. Ancient LIPs, by contrast,

46 potentially preserve a complete picture of magma storage systems and thus offer an opportunity

47 to document their structures and assess the environmental consequences.

48 　　Here we study the seismic structure of the Emeishan Large Igneous Province (ELIP) in

49 SW China based on a new surface wave tomography model. The ELIP is so far the only

50 candidate that caused a global biota crisis in the mid-Capitanian (~262 Ma) (Wignall et al.,

51 2009; Bond et al., 2019), which preceded the major volcanic activity (260-257 Ma) (Shellnutt et

52 al., 2012). We attempt to characterize the ELIP's magma storage system and address the unusual

53 asynchrony.

54

55 **GEOLOGICAL BACKGROUND**

56 　　The ELIP is located in the western Yangtze craton of the South China block (Fig.1A-B).

57 It comprises mainly tholeiitic continental flood basalts, with a lesser amount of picrites,

58 lamproites, gabbros, pyroxenites, and others (e.g., Chung and Jahn, 1995; Xu et al., 2004). These

59 rocks were mainly derived from the sub-lithospheric mantle and emplaced in the South China

60 block (Chung and Jahn, 1995; He et al., 2003; Xu et al., 2004; Zhou et al., 2005). The

61 southwestern corner of ELIP is offset left-laterally by the Cenozoic Ailao Shan-Red River shear

62 zone and poorly exposed. The larger, better preserved northeastern part, covering at least ~2.5-3

63 $\times 10^5$ km^2, is divided into three concentric zones (inner, intermediate, and outer) that represent a

64 decrease in flood basalt thickness outward (He et al., 2003; Xu et al., 2004). Before the ELIP

65 eruption, the Maokou Formation that deposited on the Yangtze carbonate platform underwent

66 erosion and karstification (He et al., 2003; Xiao et al., 2016), resulting in varying remnant

67 thickness. In particular, a NE-trending belt of anomalously thin thickness extends from the uplift

68 center to the Sichuan Basin (Fig.1C and Supplementary File).

69   Paleomagnetic studies show an equatorial paleo-latitude for the ELIP at the time of

70   eruption and an overall clockwise rotation of ~27° since 260 Ma (Huang et al., 2018). Magmatic

71   underplating occurred at the Moho depth, as evidenced by high density, high seismic wave

72   velocity, high Vp/Vs ratios, and thickened crust (Chen et al., 2015). A pronounced positive

73   residual gravity anomaly spreads from the ELIP center to the Sichuan Basin and is attributed to

74   ELIP intrusions (Deng et al., 2014).

75

76   **SURFACE WAVE TOMOGRAPHY: METHODS AND RESULTS**

77   We developed a radially anisotropic shear wave velocity model of the lithosphere under

78   the ELIP region from Rayleigh wave and Love wave phase velocity at periods of 8-167 s.

79   Rayleigh and Love waves are primarily sensitive to vertically (Vsv) and horizontally (Vsh)

80   polarized shear-wave velocities, respectively. Radial anisotropy, defined as 100%*(Vsh-Vsv)/Vs

81   where Vs is the Voigt average of Vsh and Vsv, exploits the variations between the two waves by

82   assuming hexagonal anisotropy with a vertical symmetry axis (Babuska and Cara, 1991). Radial

83   anisotropy may be induced by lattice preferred orientation of minerals such as mica, olivine, and

84   pyroxene (Shapiro et al., 2004; Silver and Chan, 1991), or by shape preferred orientation of

85   macro-scale structures such as fractures, foliation, and magma (Silver and Chan, 1988;

86   Emmermann and Lauterjung, 1997).

87   Our shear wave velocity model (Figs. 2-3 & S12-S14) shows a high velocity at 15-220

88   km depths beneath the Yangtze craton east of the Xianshuihe-Xiaojiang fault, and a low velocity

89   zone in the crust of the southeastern Tibetan Plateau. These results agree with previous studies:

90   high velocity anomaly dominates the Yangtze craton at 15-240 km depths due to the cold and

91   thick cratonic lithosphere, while the low velocity zone is related to the thickened, partially-

92   molten mid- to lower crust in Tibet (Huang et al., 2010).

93   Radial anisotropy results show profound lateral and vertical variations in the crust and

94   upper lithospheric mantle (Figs. 2-3 & S15). Positive radial anisotropy (Vsh > Vsv) is found in

95   the middle and lower crust (15 km - Moho) under the SE Tibetan Plateau, which is interpreted as

96   the sub-horizontal alignment of mica due to ductile deformation induced by the India-Asia

97   collision (Shapiro et al., 2004). Another zone of positive radial anisotropy is located around the

98   southern Xianshuihe-Xiaojiang fault. This region is also associated with low shear wave

99   velocities (Figs. 2-3 & S14-S15). We explain this as sub-horizontal ductile deformation in the

100   middle and lower crust due to the lateral expansion of the Tibetan Plateau (Copley, 2008). In the

101   lithospheric mantle below 80 km, positive radial anisotropy is present ubiquitously; similar

102   positive radial anisotropy patterns have been described from other cratons (Nettles and

103   Dziewoński, 2008). This largely results from the lattice preferred orientation of olivine in

104   horizontal planes.

105   The most intriguing phenomenon is a NE-trending coherent zone of negative radial

106   anisotropy (Vsv > Vsh) associated with a high velocity anomaly that underlies the inner and

107   intermediate zones of the ELIP (Figs. 2 & 3). It shows as a broad zone in the shallow crust (0-15

108   km) and can be traced downward to ~80 km depth. Such a zone of reduced radial anisotropy is

109   still detectable down to 120 km depth within the Yangtze craton (Figs. 2 & S15). The amplitude

110   of the negative radial anisotropy is mostly around -2% but is as strong as -4% in the lower crust

111   under the Sichuan Basin. A similar body of negative radial anisotropy was imaged, but not

112   interpreted, at 20-35 km depths by Huang et al. (2010). Another study (Xie et al., 2013) found a

113   narrow zone of negative anisotropy in the middle and upper crust under eastern Tibet and

114 ascribed it to faults and cracks. However, the presence of faults and cracks cannot explain the

115 observed combination of high velocity and negative radial anisotropy that extends into the

116 mantle lithosphere under the Sichuan Basin.

117

118 **DISCUSSION**

119 **Geological Interpretation on the High Velocity, Negative Radial Anisotropy Zone**

120 Negative radial anisotropy in the crust and upper mantle is often explained by the sub-

121 vertical alignment of mineral crystals such as mica and olivine, macroscopic structures such as

122 faults and shear zones, or partial melts (Shapiro et al., 2004; Xie et al., 2013). One explanation

123 for our case could be lithospheric-scale faulting or partial melting from the Tibetan Plateau.

124 Although it cannot be ruled out, this interpretation is not realistic because (1) the NE-trending

125 negative radial anisotropy zone is not parallel to the N-trending Xiaojiang fault, nor the NW-

126 trending Ailao Shan-Red River shear zone, (2) lithospheric-scale, high-strain structures *within*

127 the craton that could form vertical alignment are not observed, and (3) such interpretations would

128 produce low, rather than high, shear-wave velocities.

129 Noticing the southern end of the negative radial anisotropy body coincides with the

130 eruption- and domal uplift centers of the ELIP, we propose an alternative interpretation that

131 connects the seismic signature with the shape preferred orientation of magma systems (Fig. 4A).

132 A magma storage system of a LIP consists of a network of dikes, sills, laccoliths, and magma

133 chambers, by which magma is transported through and stored within the lithosphere (Ernst et al.,

134 2019). The geometry of such a system can be simplified into two end-members in the scope of

135 seismic radial anisotropy: vertical dikes, and horizontal sills. The thickness of a single dike or sill

136 is usually below the detection limit of seismic waves; in groups, however, they can be

137 seismically detectable (Backus, 1962).

138   For a transversely isotropic media of mafic to felsic compositions with a vertical or

139 horizontal symmetry (Eshelby, 1957), the presence of dikes and sills of mafic-ultramafic

140 compositions (i.e., higher Mg and Fe contents) can effectively alter the bulk elastic properties of

141 the medium (Fig. 4A). The bulk Vs and radial anisotropy of a medium with a dike-dominated

142 system both decrease at the time of intrusion; after the magma solidifies and cools, Vs increases

143 while the radial anisotropy remains depleted. For a sill-dominated system, Vs decreases first, and

144 increases after cooling, while the radial anisotropy remains elevated.

145   The observed body of negative radial anisotropy and high Vs (anomalies "a" and "c",

146 Fig. 3) can thus be interpreted as the solidified magma storage system of the ELIP that is

147 dominated by sub-seismic-scale, densely-spaced, mafic-ultramafic dikes. Field observations of

148 the ELIP dike swarm system (Li et al., 2015) support this interpretation. Anomaly "b" (Fig. 3),

149 characterized by thicker crust, higher Vs, and less-negative radial anisotropy than "a" and "c",

150 cannot be explained by a reduction of intrusions; instead, it reflects a greater amount of intrusion

151 with a higher fraction of sills.

152   One may suggest that alternatively, the paired anomaly of negative radial anisotropy and

153 high Vs may be attributed to the Neoproterozoic rifting and magmatism in South China during

154 the Rodinia breakup (Li et al., 1999). While it equally explains all the geophysical results, it

155 leaves the Permian volcanism and the erosion of Maokou Formation in the Sichuan Basin

156 unexplained (Fig. 1). Thus, we favor the Permian ELIP interpretation.

157

158 **Tectonic and Environmental Implications**

159   Tectonic reconstruction lends further support to our interpretation (Fig. 4B).

160   Paleomagnetic studies show that the South China block was moving northward around 260 Ma

161   and it has experienced an overall ~27° clockwise rotation since then (Huang et al., 2018). If the

162   Emeishan hotspot was stationary, the predicted hotspot track should align N-S in Permian, i.e.,

163   NE-SW at present. The zone of reduced radial anisotropy and high Vs at 15-120 km depths

164   trends NE through the eruption center (Fig. 2 & S15) and overlaps the positive residual gravity

165   anomaly (Deng et al., 2014). Therefore, this 700-km long anomaly represents the Emeishan

166   hotspot track that is concealed in the Yangtze craton.

167   Lithospheric thickness variations affect the route of magma transport and storage and the

168   location of eruption. A schematic section A-A" illustrates how the magma system developed

169   through time (Figs. 4C-D). In the mid- to late Guadalupian (middle Permian), a mantle upflow

170   reached the base of the thick craton and generated melt at the base of lithosphere. Its surface

171   responses include gentle uplift, erosion, and karstification of the middle-Permian Maokou

172   carbonate rocks in the Sichuan Basin; only little magma succeeded to penetrate the lithosphere

173   (Fig. 1B). As the South China block drifted northward, more melt formed and infiltrated the

174   craton, mainly as dikes. Melt at the base of the lithosphere did not find an "easy way" out until

175   the thinner margin of the Yangtze craton was above the mantle upflow. In the upper crust, the

176   Xiaojiang normal fault and the Panxi rift were (re-)activated before and during the onset of the

177   ELIP (He et al., 2003; Li et al., 2015), facilitated the erosion of Maokou Formation and the

178   magmatic emplacement.

179   Approaching the ELIP inner zone from the northeast, the radial anisotropy at "b" is not as

180   depleted as "c" under the Sichuan Basin at 15 km – Moho depth (Figs. 2 & 3), but its Vs is

181   higher. This suggests a higher fraction of sills, consistent with the magma underplating locally

182 (Chen et al., 2015) and volcanic systems in general (Jaxybulatov et al., 2014). Emplacement of

183 laterally extensive sills tends to take place in mechanical layers (Kavanagh et al., 2006) such as

184 sedimentary basins in the uppermost crust, near the brittle-ductile transition, and crust-mantle

185 interface. Sills efficiently store magma over large areas, and liberate large volumes of

186 greenhouse gases and mercury that may trigger catastrophic environmental change (Svensen et

187 al., 2009). Indeed, above "b", the 263-Ma Panzhihua layered mafic intrusions intruded and

188 metamorphosed the Dengying dolomitic limestones in the shallow crust (Zhou et al., 2005),

189 which triggered the degassing and release of mercury that caused the mid-Capitanian mass

190 extinction.

191   As the South China block kept moving northward and the major eruption occurred, the

192 release of volatiles and mercury also continued to the Guadalupian-Lopingian boundary (260

193 Ma) (Huang et al., 2019). After the magma crystallized, the ELIP strengthened the Yangtze

194 craton and controlled the geometry of the Himalayan-Tibetan orogen (Xu et al., 2020).

195   This study highlights how surface wave tomography can be used to characterize the

196 architecture of the magma storage system of LIPs and explain the relation among hotspot

197 volcanism, lithosphere, and biosphere. Similar studies can be conducted for other LIPs, which

198 may enable future models to evaluate the environment impacts in a more quantitative way.

199

206

REFERENCES CITED

208   Babuska, V., and Cara, M., 1991, Seismic anisotropy in the Earth: Kluwer, Dordrecht,

209   Netherlands, Modern Approaches in Geophysics, v. 10, 219 p.

210   Backus, G.E., 1962, Long-wave elastic anisotropy produced by horizontal layering: Journal of

211   Geophysical Research: Solid Earth, v. 67, p. 4427-4440,

212   https://doi.org/10.1029/JZ067i011p04427

213   Bond, D.P., and Wignall, P.B., 2014, Large igneous provinces and mass extinctions: an update,

214   in Keller, G., and Kerr, A.C., eds, Volcanism, Impacts, and Mass Extinctions: Causes and

215   Effects: Geological Society of America Special Papers 505, p. 29-55.

216   Bond, D.P., Wignall, P.B., and Grasby, S.E., 2019, The Capitanian (Guadalupian, Middle

217   Permian) mass extinction in NW Pangea (Borup Fiord, Arctic Canada): A global crisis

218   driven by volcanism and anoxia: Geological Society of America Bulletin, B35281.1,

219   https://doi.org/10.1130/B35281.1.

220   Bryan, S.E., and Ernst, R.E., 2008, Revised definition of large igneous provinces (LIPs): Earth-

221   Science Reviews, v. 86(1-4), p. 175-202, https://doi.org/10.1016/j.earscirev.2007.08.008.

222   Chen, Y., Xu, Y., Xu, T., Si, S., Liang, X., Tian, X., Deng, Y., Chen, L., Wang, P., Xu, Y., and

223   Lan, H., 2015, Magmatic underplating and crustal growth in the Emeishan Large Igneous

224   Province, SW China, revealed by a passive seismic experiment: Earth and Planetary

225   Science Letters, v. 432, p. 103-114, https://doi.org/10.1016/j.epsl.2015.09.048.

226   Chung, S.L., and Jahn, B.M., 1995, Plume-lithosphere interaction in generation of the Emeishan

227   flood basalts at the Permian-Triassic boundary: Geology, v. 23(10), p. 889-892,

228   https://doi.org/10.1130/0091-7613(1995)023<0889:PLIIGO>2.3.CO;2.

229 Copley, A., 2008, Kinematics and dynamics of the southeastern margin of the Tibetan Plateau:

230   Geophysical Journal International, v. 174(3), p. 1081-1100,

231   https://doi.org/10.1111/j.1365-246X.2008.03853.x.

232 Deng, Y., Zhang, Z., Mooney, W., Badal, J., Fan, W., and Zhong, Q., 2014, Mantle origin of the

233   Emeishan large igneous province (South China) from the analysis of residual gravity

234   anomalies: Lithos, v. 204, p. 4-13. https://doi.org/10.1016/j.lithos.2014.02.008

235 Emmermann, R., and Lauterjung, J., 1997, The German continental deep drilling program KTB:

236   overview and major results: Journal of Geophysical Research: Solid Earth, v. 102(B8), p.

237   18179-18201, https://doi.org/10.1029/96JB03945.

238 Ernst, R.E., 2014, Large Igneous Provinces: Cambridge University Press, 653 p.

239 Ernst, R.E., Liikane, D.A., Jowitt, S.M., Buchan, K.L., and Blanchard, J.A., 2019, A new

240   plumbing system framework for mantle plume-related continental Large Igneous

241   Provinces and their mafic-ultramafic intrusions: Journal of Volcanology and Geothermal

242   Research, v. 384, p. 75-84. https://doi.org/10.1016/j.jvolgeores.2019.07.007.

243 Eshelby, J.D., 1957. The determination of the elastic field of an ellipsoidal inclusion, and related

244   problems. Proceedings of the Royal Society of London, ser. A, v. 241(1226), p. 376-396,

245   https://doi.org/10.1098/rspa.1957.0133.

246 He, B., Xu, Y.G., Chung, S.L., Xiao, L., and Wang, Y., 2003, Sedimentary evidence for a rapid,

247   kilometer-scale crustal doming prior to the eruption of the Emeishan flood basalts: Earth

248   and Planetary Science Letters, v. 213(3-4), p. 391-405, https://doi.org/10.1016/S0012-

249   821X(03)00323-6.

250 Huang, B., Yan, Y., Piper, J.D., Zhang, D., Yi, Z., Yu, S., and Zhou, T., 2018, Paleomagnetic

251   constraints on the paleogeography of the East Asian blocks during Late Paleozoic and

252   Early Mesozoic times: Earth-Science Reviews, v. 186, p. 8-36,

253   https://doi.org/10.1016/j.earscirev.2018.02.004.

254 Huang, H., Yao, H., and van der Hilst, R.D., 2010, Radial anisotropy in the crust of SE Tibet and

255   SW China from ambient noise interferometry: Geophysical Research Letters, v. 37(21),

256   L21310, https://doi.org/10.1029/2010GL044981

257 Huang, Y., Chen, Z.Q., Wignall, P.B., Grasby, S.E., Zhao, L., Wang, X., and Kaiho, K., 2019,

258   Biotic responses to volatile volcanism and environmental stresses over the Guadalupian-

259   Lopingian (Permian) transition: Geology, v. 47(2), p. 175-178,

260   https://doi.org/10.1130/G45283.1.

261 Jaxybulatov, K., Shapiro, N.M., Koulakov, I., Mordret, A., Landès, M., and Sens-Schoenfelder,

262   C., 2014, A large magmatic sill complex beneath the Toba caldera: Science, v.

263   346(6209), p. 617-619, https://doi.org/10.1126/science.1258582.

264 Jiang, C., Schmandt, B., Farrell, J., Lin, F.C., and Ward, K.M., 2018, Seismically anisotropic

265   magma reservoirs underlying silicic calderas: Geology, v. 46(8), p. 727-730,

266   https://doi.org/10.1130/G45104.1.

267 Kavanagh, J.L., Menand, T., and Sparks, R.S.J., 2006, An experimental investigation of sill

268   formation and propagation in layered elastic media: Earth and Planetary Science Letters,

269   v. 245(3-4), p. 799-813, https://doi.org/10.1016/j.epsl.2006.03.025.

270 Li, H., Zhang, Z., Ernst, R., Lü, L., Santosh, M., Zhang, D., and Cheng, Z., 2015, Giant radiating

271   mafic dyke swarm of the Emeishan Large Igneous Province: Identifying the mantle

272   plume centre: Terra Nova, v. 27(4), p. 247-257, https://doi.org/10.1111/ter.12154.

273 Li, Z.X., Li, X.H., Kinny, P.D., and Wang, J., 1999. The breakup of Rodinia: did it start with a

274   mantle plume beneath South China?: Earth and Planetary Science Letters, v. 173(3), p.

275   171-181. https://doi.org/10.1016/S0012-821X(99)00240-X.

276 Nettles, M., and Dziewoński, A.M., 2008, Radially anisotropic shear velocity structure of the

277   upper mantle globally and beneath North America: Journal of Geophysical Research:

278   Solid Earth, v. 113(B2), B02303, https://doi.org/10.1029/2006JB004819.

279 Shapiro, N.M., Ritzwoller, M.H., Molnar, P., and Levin, V., 2004, Thinning and flow of Tibetan

280   crust constrained by seismic anisotropy: Science, v. 305(5681), p. 233-236,

281   https://doi.org/10.1126/science.1098276.

282 Shellnutt, J.G., Denyszyn, S.W., and Mundil, R., 2012, Precise age determination of mafic and

283   felsic intrusive rocks from the Permian Emeishan large igneous province (SW China):

284   Gondwana Research, v. 22(1), p. 118-126, https://doi.org/10.1016/j.gr.2011.10.009.

285 Silver, P.G., and Chan, W.W., 1988, Implications for continental structure and evolution from

286   seismic anisotropy: Nature, v. 335(6185), p. 34-39, https://doi.org/10.1038/335034a0.

287 Silver, P.G., and Chan, W.W., 1991, Shear wave splitting and subcontinental mantle

288   deformation: Journal of Geophysical Research: Solid Earth, v. 96(B10), p. 16429-16454,

289   https://doi.org/10.1029/91JB00899.

290 Sobolev, S.V., Sobolev, A.V., Kuzmin, D.V., Krivolutskaya, N.A., Petrunin, A.G., Arndt, N.T.,

291   Radko, V.A., and Vasiliev, Y.R., 2011, Linking mantle plumes, large igneous provinces

292   and environmental catastrophes: Nature, v. 477(7364), p. 312-316,

293   https://doi.org/10.1038/nature10385.

294 Svensen, H., Planke, S., Polozov, A.G., Schmidbauer, N., Corfu, F., Podladchikov, Y.Y., and

295   Jamtveit, B., 2009, Siberian gas venting and the end-Permian environmental crisis: Earth

296   and Planetary Science Letters, v. 277(3-4), p. 490-500.

297   https://doi.org/10.1016/j.epsl.2008.11.015.

298   Wignall, P.B., Sun, Y., Bond, D.P., Izon, G., Newton, R.J., Védrine, S., Widdowson, M., Ali,

299   J.R., Lai, X., Jiang, H., and Cope, H., 2009, Volcanism, mass extinction, and carbon

300   isotope fluctuations in the Middle Permian of China: Science, v. 324(5931), p. 1179-

301   1182, https://doi.org/10.1126/science.1171956.

302   Xiao, D., Tan, X., Xi, A., Liu, H., Shan, S., Xia, J., Cheng, Y., and Lian, C., 2016, An inland

303   facies-controlled eogenetic karst of the carbonate reservoir in the Middle Permian

304   Maokou Formation, southern Sichuan Basin, SW China: Marine and Petroleum Geology,

305   v. 72, p. 218-233. https://doi.org/10.1016/j.marpetgeo.2016.02.001.

306   Xie, J., Ritzwoller, M.H., Shen, W., Yang, Y., Zheng, Y., and Zhou, L., 2013, Crustal radial

307   anisotropy across eastern Tibet and the western Yangtze craton: Journal of Geophysical

308   Research: Solid Earth, v. 118(8), p. 4226-4252, https://doi.org/10.1002/jgrb.50296.

309   Xu, X., Zuza, A.V., Yin, A., Lin, X., Chen, H., and Yang, S., 2020. Permian plume-strengthened

310   Tarim lithosphere controls the Cenozoic deformation pattern of the Himalayan-Tibetan

311   orogen: Geology, v. 49. https://doi.org/10.1130/G47961.1.

312   Xu, Y.G., He, B., Chung, S.L., Menzies, M.A., and Frey, F.A., 2004, Geologic, geochemical,

313   and geophysical consequences of plume involvement in the Emeishan flood-basalt

314   province: Geology, v. 32(10), p. 917-920, https://doi.org/10.1130/G20602.1.

315   Zhou, M.F., Robinson, P.T., Lesher, C.M., Keays, R.R., Zhang, C.J., and Malpas, J., 2005,

316   Geochemistry, petrogenesis and metallogenesis of the Panzhihua gabbroic layered

317   intrusion and associated Fe-Ti-V oxide deposits, Sichuan Province, SW China: Journal of

318   Petrology, v. 46(11), p. 2253-2280, https://doi.org/10.1093/petrology/egi054.

319

320 FIGURE CAPTIONS

321 Figure 1. Geologic map of the Emeishan Large Igneous Province (ELIP). (A) Index map. IC,

322 Indochina; IN, India Plate; NC, North China; SC, South China; TP, Tibetan Plateau. (B) Map of

323 the ELIP, showing eruption center, uplift center, flood basalts exposed on surface and drilled in

324 wells, buried volcanic craters, basaltic dikes, and borders of the inner (I),intermediate (II), and

325 outer (III) zones. ASRRSZ, Ailao Shan-Red River Shear Zone; LMST, Longmen Shan thrust

326 belt; XXF, Xianshuihe-Xiaojiang Fault. (C) Isopach map of the remnant Maokou Formation

327 deposited on the Yangtze carbonate platform prior to the ELIP. Additional contours of 160 and

328 250 m are shown as dashed lines. See Supplementary File for data sources.

329

330 Figure 2. 3-D isotropic shear wave velocity models (Vs) (A-E) and radial anisotropy (γ) (F-J)

331 beneath the ELIP at depths of 0-100 km. Shear wave velocity (Vs) is calculated via a Voigt

332 average $V_S = \sqrt{(2V_{sv}^2 + V_{sh}^2)/3}$ and radial seismic anisotropy is defined as the percentage

333 difference between Vsh and Vsv in the medium: γ = (Vsh−Vsv)/Vs. TP, Tibetan Plateau; YZC,

334 Yangtze Craton.

335

336 Figure 3. Cross-section AA' showing (A) topography, (B) absolute isotropic Vs, and (C) radial

337 seismic anisotropy. Location of AA' is shown in Fig. 2. Anomalies "a", "b", and "c" are

338 discussed in the text.

339

340 Figure 4. Geologic interpretations. (A) Effects of mafic-ultramafic magma systems on seismic

341 properties (bulk shear-wave velocity and radial anisotropy) due to different geometry and

342   temperature. (B) Plate reconstruction at 260 Ma (after Huang et al. 2018) with plate boundaries

343   and velocity vectors. The South China block is highlighted in yellow. Red dashed line indicates

344   the inferred hotspot track and the location of transect A-A" that contains our seismic image A-

345   A'. (C) Integrated section along the Emeishan hotspot track. Dikes, sills, flood basalts, and faults

346   are not to scale. (D) Cartoons along A-A", showing northward-drifting Yangtze craton, mantle

347   upflow, intrusions, and surface uplift (not to scale).

348

349

350   [1]GSA Data Repository item 202Xxxx, Methods, notes, and supplementary figures, is available

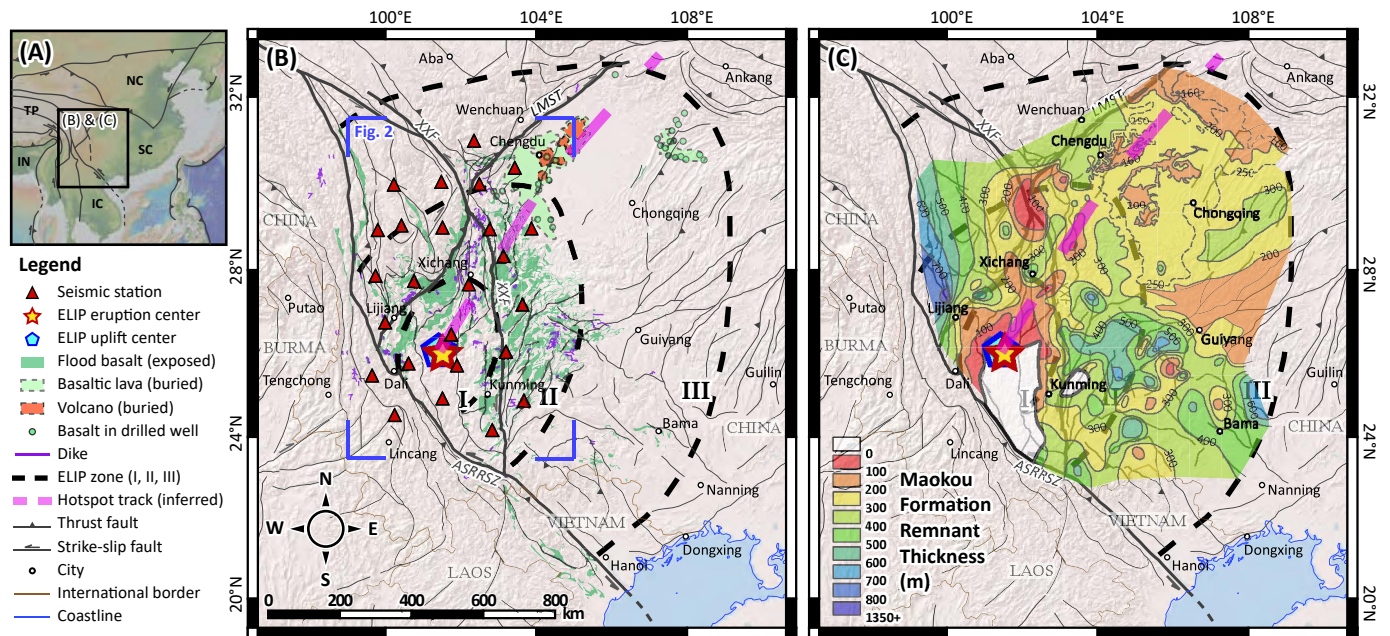351   online at www.geosociety.org/pubs/ft20XX.htm, or on request from editing@geosociety.org.
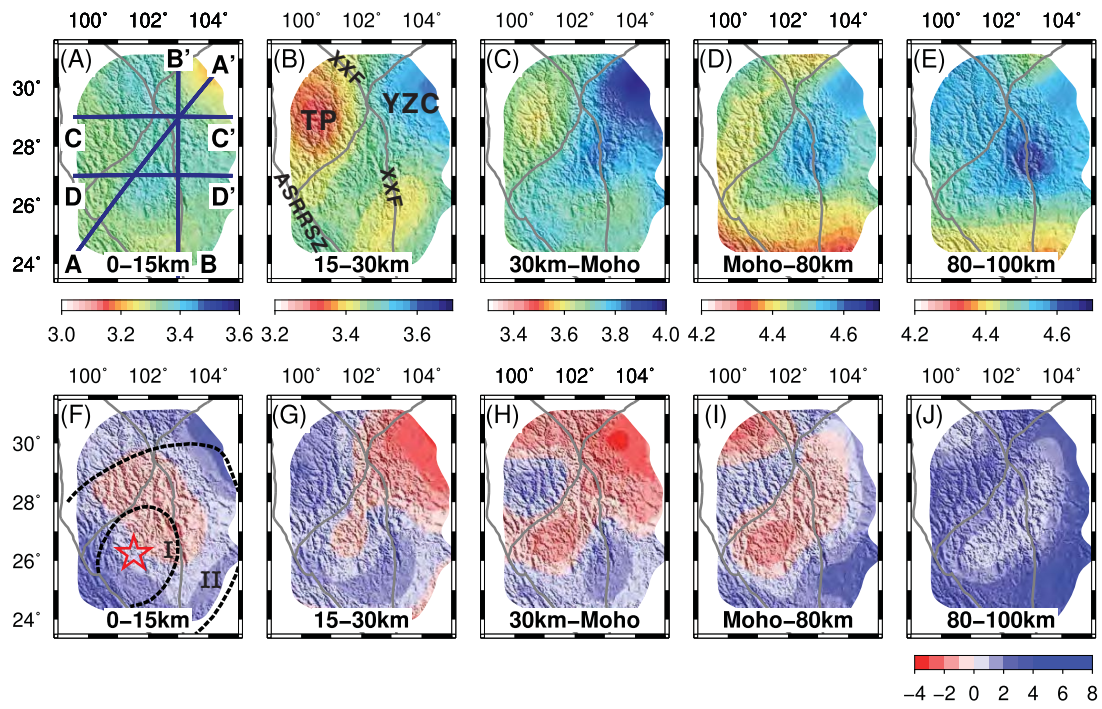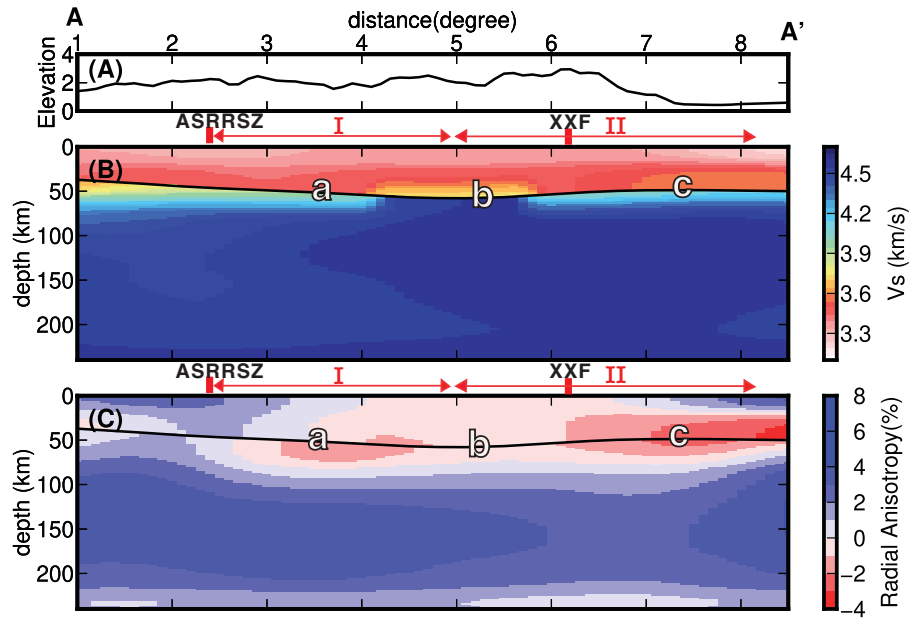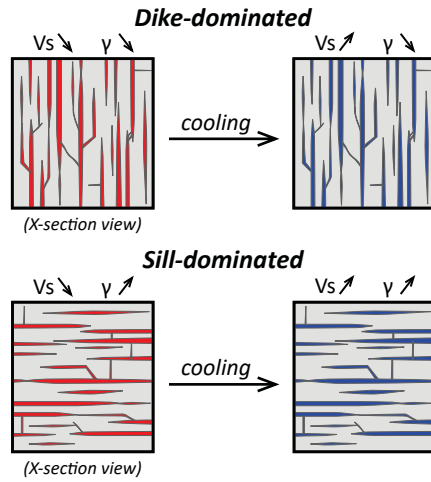
Figure 1

Figure 2

Figure 3

Figure 4

(A) Effects of mafic-ultramafic intrusions

Dike-dominated

Vs ↘ γ ↘ → *cooling* → Vs ↗ γ ↘

(X-section view)

Sill-dominated

Vs ↘ γ ↗ → *cooling* → Vs ↗ γ ↗

(X-section view)

(B) Plate reconstruction at 260 Ma

↑ 5 cm/yr

Mongol-Okhotsk

Paleo-Tethys

NC

SC

present-day graticule

Panthalassa
(Paleo-Pacific)

Emeishan hotspot track & ELIP
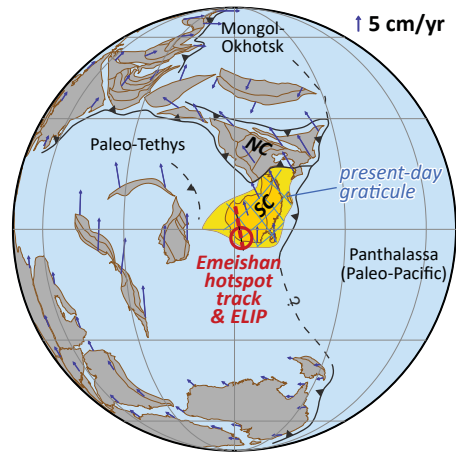
(C) Present-day observation & interpretation

→ **NE at Present (near N in Permian)**

Major uplift & eruption, 260 Ma

Degassing & mass extinction, 262 Ma

Gentle uplift & rifting, uneven erosion & paleo-karst, mid- to late-Guadalupian

A   ASRRSZ   XXF   A'   A"

offset by ASRRSZ

a   b   c

Moho

not imaged

Depth (km)

0   100   200   300

LAB

V:H = 1
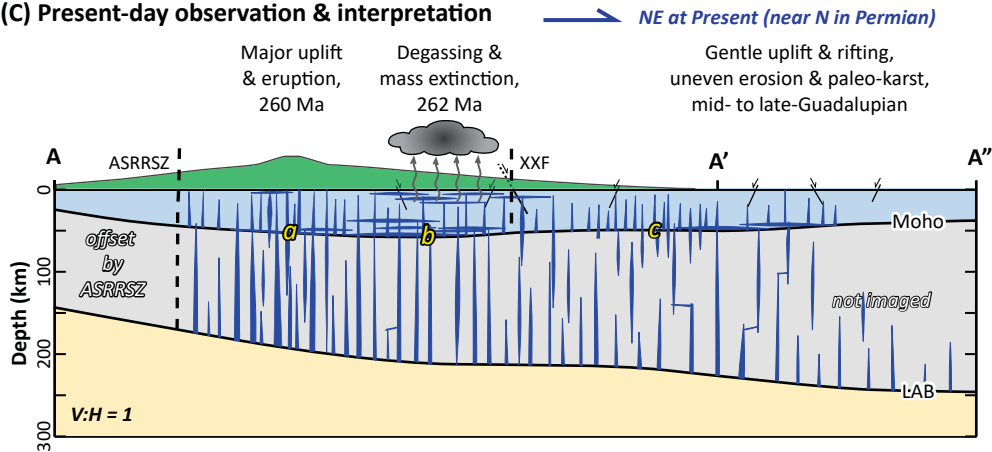
(D) ELIP evolution in Middle Permian

→ **SCB plate motion (near N in Permian)**

265(?) Ma

surface uplift

Moho

LAB

Depth (km)
0   100   200   300

V:H = 2   **mantle upflow**

262 Ma

260 Ma